Directed-Energy Laser-Thermal Propulsion for Rapid Transit Missions

Author: Zhuo Fan Bao

Supervisor: Prof. Andrew Higgins

A thesis submitted to McGill University in partial fulfilment of the requirements of the Undergraduate Honours Program.

Department of Mechanical Engineering

McGill University

Canada

December 3, 2019

Abstract

In light of recent development in fiber optic lasers, laser thermal propulsion as a potential candidate for fast interplanetary missions is investigated. This study acknowledges the need for both high specific impulse and high thrust propulsion methods to unlock our solar system and investigates the coupling of laser radiation to a working fluid to generate thrust. Modelling using a fluid simulation approach as well as a Monte Carlo approach were conducted in order to demonstrate the ability of a laser thermal rocket to attain significantly high ΔV values to enable fast interplanetary travel. Through numerical methods, it was proven that the specific impulse of laser thermal propulsion can be bounded on the order of 1000 s, showing great promise for future development of this technology.

Compte-tenu de développements récents de lasers à fibres-optiques, la propulsion thermique au laser est étudiée en tant que candidate potentielle pour des missions interplanétaires rapides. Cette étude reconnaît le besoin de moteurs-fusées à impulsion spécifique élevée et à forte poussée pour faciliter l'exploration de notre système solaire. Elle étudie le couplage du rayonnement laser à un fluide de travail. Une modélisation utilisant une approche de simulation des fluides ainsi qu'une approche de Monte Carlo a été réalisée afin de démontrer la capacité d'une fusée thermo-laser à atteindre des valeurs ΔV significativement élevées pour permettre des déplacements interplanétaires rapides. Par des méthodes numériques, il a été prouvé que l'impulsion spécifique de la propulsion thermique au laser pouvait être limitée à l'ordre de 1000 s, ce qui est très prometteur pour le développement futur de cette technologie.

Acknowledgements

The author thanks Andrew Higgins for his guidance and for always sharing his passion for space with others. The author would also like to thank Philip Lubin, Carl Knowlen, Mélanie Tétreault-Friend, XiaoCheng Mi, Abtin Ameri, and Emmanuel Duplay for providing valuable insight and feedback.

Contents

Chapter 1

Introduction

Improvements in fiber laser technology has allowed the price and power of fiber optic lasers to significantly improve over the past decade in a Moore's law fashion. This has contributed to the development of cheap, modular and scalable laser array systems that can phase-lock together to act as a single optical element of considerably large dimensions that could be disruptive for deep-space propulsion. The scalable laser array is able to accomplish a wide variety of missions by delivering directed energy to spacecrafts, which allows them to forego the need to carry power sources, and even reaction mass, on board. For example, application of direct photon pressure onto a one-meter lightsail can propel an ultra-low mass "wafersat" to 20% the speed of light within a few minutes using a large (~ 10 km) laser array focusing 100 GW/m^2, paving the way for true interstellar flight [1].

Alternatively, more modest arrays can provide power to mass reaction propulsion spacecrafts to execute payload, and potentially even human missions, within the solar system at high ΔV. For instance, it can provide power to electric propulsion thrusters with high-efficiency solar cells tuned to the laser frequency at fluxes on the order of 10 kW/m^2 (i.e., ten "suns"). In a 2018 NIAC study [2], Brophy et al. discussed the preliminary design of this propulsion architecture, targeting a maximum velocity of more than 40 AU per year given a kilometer-scale 100 MW laser array and a 40,000 s specific impulse lithium-ion thruster.

This system is well matched for interstellar precursor missions—long duration (several years) transits to the outer edge of the solar system, targeting the interstellar medium or the solar gravitational focus (550 AU). Ultra-high specific impulse is less well suited to fast interplanetary missions, such as Earth-to-Mars transit in a month, due to the inherent low-thrust associated with electric propulsion systems, which translates into long acceleration maneuver periods. Furthermore, kilometer-scale arrays represent a significant technological leap that is unlikely to be the first demonstration of directed energy propulsion.

Laser thermal propulsion, a high thrust propulsion method with moderate specific impulse between chemical and electric propulsion, is another potential approach to directed energy applications. Lightweight and highly reflective parabolic concentrators can focus the incoming laser radiation into a heating chamber where a working fluid, likely hydrogen, is heated to ionization temperatures and acts as a energy conversion system to convert laser energy into enthalpy, which is then expanded through a conventional nozzle to provide thrust. The combination of a lack of onboard oxidizer and power source, of the potential ability to operate at very high power and thrust levels, and the simple and lightweight hardware onboard can allow laser thermal propulsion to be well suited for rapid interplanetary travel [3], [4].

Laser thermal propulsion was extensively studied in the 1970s and 1980s, where CO_2 lasers operating at 10.6 μm were usually assumed as the laser source [5], [6]. The use of longer wavelength and meter-scale optics would limit the application to either earth-to-orbit launch for small vehicles (due to power limitations) or orbit raising from low earth orbit (LEO). The distance a laser of optical diameter d can deliver energy to a target of size D is of the order of $\frac{dD}{\lambda}$; a 1-m-diameter laser operating at 10 μm would only be able to focus energy onto a 10-m-diameter receiver to a distance on the order of 1000 km (i.e., LEO). The present study considers the implications of revisiting the laser thermal propulsion concept using 1-μm-wavelength fiber-optic lasers operating as a dense phased array with dimensions of order 10 m in diameter, and thus able to deliver energy to 100,000 km. The earlier research on laser thermal propulsion provides a basis that informs the present study.

Laser thermal propulsion directly deposits energy into the propellant, which is then exhausted through a thrust conversion system [7]. Laser thermal propulsion operates in two different regimes—repetitively pulsed and continuous wave. Repetitively pulsed (RP) laser propulsion uses a pulsed laser of very great fluence to ablate the propellant and to superheat it to form plasma [7], [8]. This method requires the pulse frequency to be synchronized with the propellant and a laser capable of producing very high fluence [8]. The present study is, in contrast, focused on the propulsion applications of continuous wave (CW) lasers, as this approach is well-suited to the phased array of fiber-based lasers approach.

Continuous wave (CW) laser propulsion heats the propellant and sustains a steady-state plasma. For hydrogen, CW laser propulsion can operate at laser intensities above the maintenance threshold ($2.6 \times 10^4 - 29.5 \times 10^4$ W/cm^2) as predicted numerically by Jackson and Nielsen [9] and experimentally by Conrad et al. [5], but faces absorption zone instabilities that can hinder plasma generation [4], [8].

The present study is a revisit of the concept of laser thermal propulsion in light of the developments in fiber-optic lasers. It will focus on CW laser propulsion for rapid transit missions in the solar system.

Chapter 2

Thrust Optimization

Fundamental considerations of thrust and specific impulse can help to match propulsion technologies and missions. CW laser thermal rockets exhaust at a constant mass flow rate. The total change of spacecraft velocity, ΔV, is given by the rocket equation

$$\Delta V = I_{\mathrm{sp}}\; g_0\; \ln\frac{m_{\mathrm{i}}}{m_{\mathrm{f}}} \text{ (Ref. [10], [11])}, \tag{2.1}$$

where I_{sp} is the specific impulse, g_0 is the gravitational constant, and $\frac{m_{\mathrm{i}}}{m_{\mathrm{f}}}$ is the initial (entire vehicle) to final (entire vehicle without the propellant) mass ratio of the spacecraft.

In order to perform missions such as 30-45 days to Mars, one year to Jupiter or 20 years to the solar gravitational focus, a ΔV of around 30 km/s is necessary. To achieve ΔVs on that order of magnitude, mass ratio $\frac{m_{\mathrm{i}}}{m_{\mathrm{f}}}$ and I_{sp} would need to be maximized. Due to physical limitations of a rocket not being able to be entirely made out of propellant, the mass ratio optimization is limited despite the advantage gained by eliminating oxidizer and a power source on board the rocket. Thus, the only parameter in the rocket equation left to optimize is I_{sp}, the efficiency of the propellant. A higher I_{sp} would translate to higher ΔVs possible for a rocket with the same mass ratio. I_{sp} depends on the exhaust gas temperature (T_{e}) and molecular weight (MW) of the propellant in a square root fashion

$$I_{\mathrm{sp}} \sim \sqrt{\frac{T_{\mathrm{e}}}{\mathrm{MW}}} \text{ (Ref. [4])} \tag{2.2}$$

Currently, the best chemical hydrogen-oxygen rockets have an I_{sp} of about 450 s because the reaction is limited to temperatures of around 3500 K and creates products of around 12 kg/kmol molecular weight [4]. On the other hand, owing to high chamber temperature and low propellant molecular weight, laser thermal propulsion rockets can theoretically achieve a specific impulse beyond 1000 s, making it a very desirable option for rapid interplanetary transits.

I_{sp}, although important, is not the only parameter that should be considered in optimization. Especially for short duration missions such as a 30-45 days Mars flyby, time limitations must also be factored into consideration. For power-constrained spacecraft, there exists a trade-off between thrust and I_{sp} as shown in the following equation:

$$P_{\mathrm{r}} = \frac{F \; I_{\mathrm{sp}} \; g_0}{2 \; \eta} \text{ (Ref. [4])}, \tag{2.3}$$

where P_{r} is power input to the rocket, F is thrust, and η is thrust conversion efficiency.

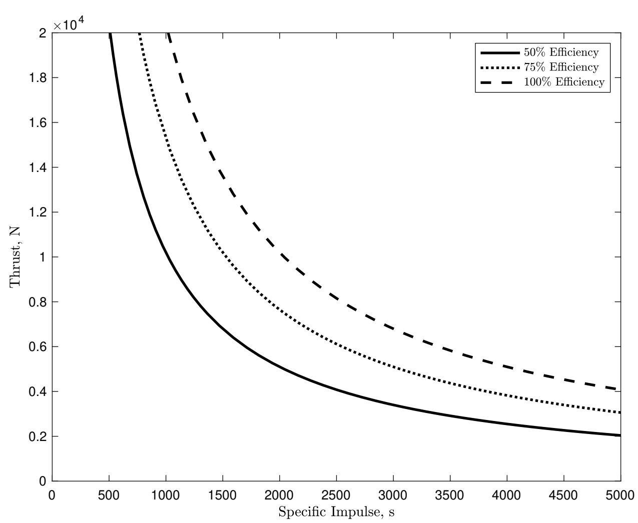

Figure 2.1: Power-limited rocket thrust and specific impulse trade-off.

As seen in Fig. 2.1, the trade-off for high I_{sp} is low thrust, which translates to longer acceleration and laser beam operation times. For example, ion electric propulsion features impressive specific impulse on the order of several thousands of seconds at the expense of lower thrust, and therefore would take almost 10 days to reach the necessary ΔV. While this regime is valuable for long term missions where a 10-day acceleration time is negligible, higher I_{sp} is not suitable for rapid interplanetary missions due to time and technical limitations:

- Shorter acceleration time implies laser near field limit can be closer to launch site, which implies the vehicle can be accelerated using a small laser array (on the order of 10 m) and act as a proof of concept mission.

- Longer acceleration times associated with laser-electric propulsion also imply that several laser arrays would need to be built world-wide (similar to the Deep Space Network) or the laser array might need to be constructed in space in order to continuously beam to the spacecraft over long periods of time.

- Shorter acceleration times per mission allows for greater mission frequency. E.g., several missions could be launched by a single laser array during a launch opportunity of planetary alignment.

Stuhlinger derived an optimization method that maximizes payload mass and determines the I_{sp} as a function of propellant burn time

$$v_{\mathrm{ch}} = \sqrt{\frac{2\ \eta\ t_{\mathrm{b}}}{\alpha}} \text{ (Ref. [12])}, \tag{2.4}$$

where η is the thrust conversion efficiency, t_{b} is the propellant burn time, α is the specific power and v_{ch} is the Stuhlinger velocity, which is the velocity the exhaust would achieve by converting all the available energy to thrust at a constant rate within the burn time. Figure 2.2 shows that as burn time shortens; specific impulse must decrease to provide enough acceleration. It also illustrates the necessity of an α of around 0.01 kg/kW to accelerate to the necessary ΔV in a constrained burn time.

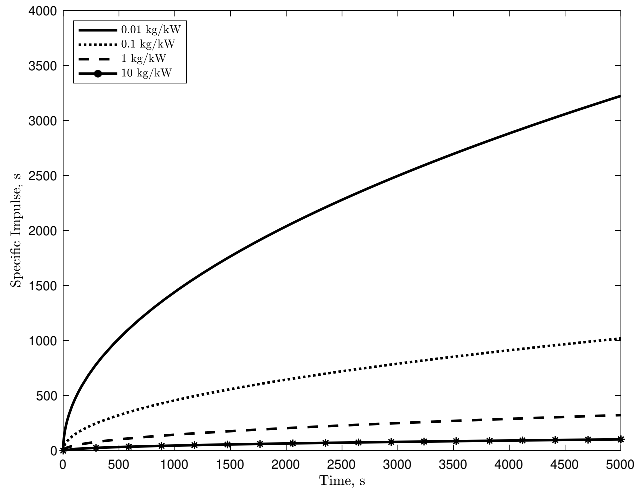

Figure 2.2: Stuhlinger optimized specific impulse in terms of burn time.

2.1 Specific Impulse Considerations

For laser-heating chambers exceeding 5000 K, the hydrogen is expected to be fully dissociated, and for temperatures approaching 20,000 K, the hydrogen will be fully ionized. As both dissociated and ionized hydrogen is monatomic, this feature enables a simple estimate of exhaust velocity assuming the chemical composition remains fixed (i.e., frozen flow) through the expansion process. From conservation of energy

$$h_0 = h + \frac{v^2}{2} \tag{2.5}$$

For a monatomic gas of fixed composition, $h = c_p T = \frac{5}{2}\frac{R_\mathrm{u}}{\mathrm{MW}}T$, so the exhaust velocity is given by

$$V_{\mathrm{exit}_{\mathrm{frozen}}} = \sqrt{2(h_0 - h_{\mathrm{exit}})} = \sqrt{5\frac{R_\mathrm{u}}{\mathrm{MW}}\left(T_0 - T_{\mathrm{exit}}\right)} \tag{2.6}$$

This value of exhaust velocity is plotted in Fig. 2.3, normalized by g_0, assuming complete expansion of products to vacuum, as a function of the heating chamber temperature.

In practice, as the hydrogen expands and cools, recombination to atomic and then molecular hydrogen will release additional energy into the flow. This is accounted for by including

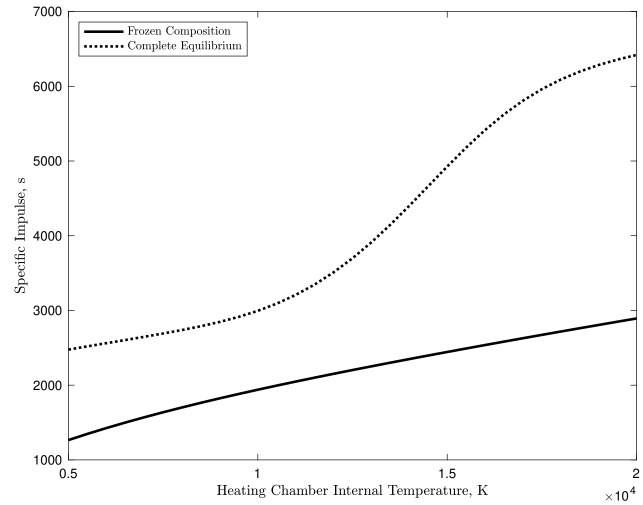

Figure 2.3: Specific impulse based on expansion from chamber temperature.

the enthalpy of formation as follows

$$h_0 = h^0_{\mathrm{f_H}} + \alpha_0 \; h^0_{\mathrm{f_{H+}}} + c_{p\ \mathrm{diatomic}}(T_0 - T_{\mathrm{ref}}) = h^0_{\mathrm{f_{H_2}}} + c_{p\ \mathrm{monatomic}}(T_{\mathrm{exit}} - T_{\mathrm{ref}}) + \frac{v^2_{\mathrm{exit}}}{2} \tag{2.7}$$

where α is the ionization fraction given by Eq. A.9 or Eq. A.10 (Ref. [13]) and complete recombination has been assumed in the exhaust products. The enthalpy of formation terms h^0_{f} takes into account the energy released in electron recombination and the forming of chemical bonds; $h^0_{\mathrm{f_{H_2}}} = 0$ by definition. Solving for exhaust velocity

$$V_{\mathrm{exit_{equilibrium}}} = \sqrt{2(h^0_{\mathrm{f_H}} + \alpha_0 \; h^0_{\mathrm{f_{H+}}}) + 5\frac{R_{\mathrm{u}}}{\mathrm{MW}}\,(T_0 - T_{\mathrm{ref}}) - 7\frac{R_{\mathrm{u}}}{\mathrm{MW}}\,(T_{\mathrm{exit}} - T_{\mathrm{ref}})} \tag{2.8}$$

which is also plotted in Fig. 2.3 for case of complete expansion to vacuum.

The two solutions plotted in Fig. 2.3 represent the specific impulse for the two cases considered here (frozen and equilibrium flow) and should bound the actual performance of a laser thermal propulsion system, minus additional losses.

Chapter 3

Laser Sustained Plasma

The heating chamber, the crux of a laser thermal rocket, converts the delivered laser energy into enthalpy for the nozzle to expand. A plasma, located in the center of the heating chamber, absorbs the laser radiation and acts as an energy conversion system.

To minimize energy lost, it is crucial to understand the absorption and emission mechanisms as well as heat transfer processes inside the chamber. In this chapter, the physics of the laser deposition process is reviewed.

3.1 Absorption/Emission Mechanisms

Gas emission and absorption are the result of electronic transitions between energy states. The absorption of a photon is always accompanied by the excitation of the system to a higher energy state, while emission can only occur to already excited systems as the energy is transferred to the emitted photon and as the electron drops to a lower energy state. Furthermore, in the case of high temperature gas, ionization is more likely, allowing the electrons to reach a free energy state where any energy value is possible (continuous energy states).

The transition of electrons between these different energy states can be separated into three different groups that can help explain emission and absorption: bound-bound, bound-free and free-free transitions.

Bound-bound transitions refer exclusively to the transitions between the discrete energy levels and are responsible for the line absorption and emission. On the other hand, bound-free and free-free transitions contribute to the continuum absorption and emission of the gas because they take place within a continuous range of energy states.

Due to the narrow wavelength range of bound-bound transitions, they do not contribute significantly to the overall absorption and emission of the gas in comparison to continuum absorption and emission, which can sometimes lead to bound-bound transitions being disregarded from consideration. Such will be the case for the radiation loss in this modelling attempt.

In the subsections below, the mechanisms that dominate for energy exchange inside the heating chamber are considered. The calculations for the absorption and emission coefficients can be found in the appendix.

3.1.1 Absorption

In the case of hydrogen plasma sustained by 1 μm laser radiation, absorption exchanges are dominated by free-free transitions (inverse bremsstrahlung) where gases absorb radiation in a non-resonant fashion using free electrons. The contribution from bound-free (photoionization) and free-free (line absorption) transitions are near insignificant in comparison because resonance between the light and hydrogen gas is required for photoionization and line absorption. Unfortunately, hydrogen gas is not resonant with 1 μm laser light, which severely hinders contribution from bound transitions [14].

3.1.2 Emission

Hot hydrogen gas emits at all wavelengths, and thus all emission mechanisms should be considered. However, due to its discrete nature, line emission contribution to radiation loss is minimal. As can be seen in Figure 3.1, compared to blackbody emission at 20000 K, line emission can only contribute a very small fraction of the total power, and neglecting it will not significantly affect the model as most emission power comes from bound-free and free-free transitions that emit continuously. In the context of this model, consideration for emission

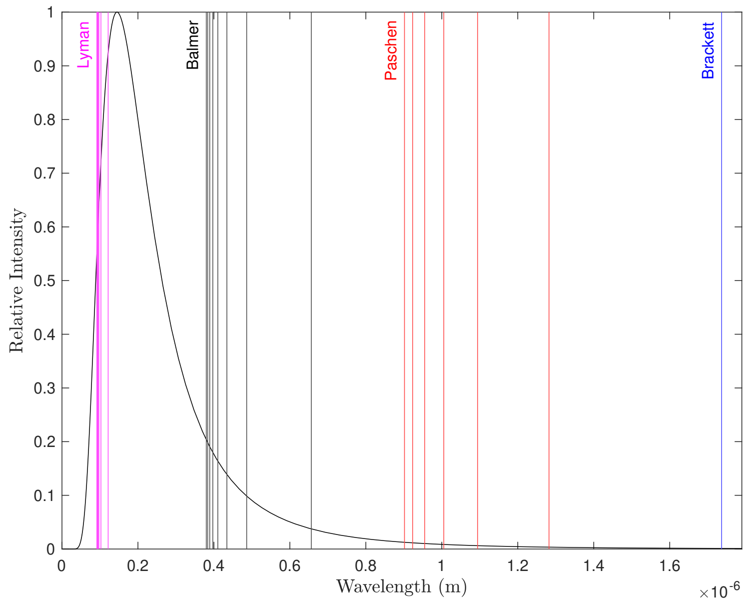

Figure 3.1: Blackbody Emission Comparison with Hydrogen Line Emission at 20000 K

will only be given to photoelectric and bremsstrahlung effects.

3.2 Transient State

Lasers can generate or sustain plasmas in various different ways that depend on the intensity, spot size, and mode of operation of the laser beam and on the propellant gas conditions. High energy repetitively pulsed (RP) lasers can directly cause breakdown within the gas by ablating the propellant similar to an explosion, but CW lasers can only provide enough energy to sustain the plasma in a continuous fashion and would need a secondary source to initialize plasma breakdown.

Consideration for plasma generation is limited because the transient plasma development process is not well understood and falls beyond the scope of laser supported plasma.

After breakdown, a plasma can propagate to the surrounding cold gas in three different ways: laser-supported combustion (LSC), laser-supported detonation (LSD), and laser-supported radiation (LSR) absorption waves. The propagation method can heavily influence the final steady-state plasma.

The LSC wave appears in low intensity sustained plasmas because it only requires maintenance threshold laser intensity to stabilize. The ambient gas is heated by passing through a precursor shock and by the radiation of the already formed plasma. The LSD wave is a regime, situated in between LSC and LSR, where the precursor shock itself is able to heat the gas to initiate absorption. LSD waves operate at higher temperatures and laser intensities than LSC waves: the transition happens between 5-20 MW/cm^2 and seems to be largely wavelength independent. At higher laser intensities, the plasma radiation itself is strong enough to heat the ambient gas to initiate laser absorption. This is referred to as the LSR wave regime where the plasma temperature is on the order of 100,000 K and requires nearly 1 GW/cm^2 of laser intensity to be sustained [14].

To accomplish the various missions discussed in the Introduction, LSC waves are the most optimal regime to operate the rocket in because they require a lower intensity to maintain and do not radiate excessively outwards. The ideal plasma should be as large as possible without excessive thermal loads to the walls of the heating chamber. LSD and LSR waves both reach too high temperatures, thus increasing its radiation and require a laser flux that would overly constrain plasma size.

3.3 Steady State

The constant pressure expanding LSC wave will eventually reach steady-state as it expands along the laser beam to a point where laser absorption and heat loss reach a balance. One- [15], [16] and two-dimensional [17], [18] models of the LSC wave have been developed in the past, but all assumed a CO_2 10.6 μm laser as the directed energy source and worked with argon gas. This study revisits the previous studies on steady state LSC waves but applied to 1-μm fiber optic lasers radiating onto hydrogen gas.

3.3.1 One-Dimension LSC

Steady-state solutions in one-dimension, while accurate to a certain extent, can not account for the two-dimensional nature of a laser beam profile. A laser beam profile is by nature non-uniform. The intensity of the beam increases radially towards the middle of the beam.

This study will attempt to couple a converging beam profile to a two-dimensional LSC model to obtain its temperature profile.

3.3.2 Two-Dimension LSC

For a constant pressure cylindrical heating chamber, the model can be simplified to a two-dimensional profile (Figure 3.2) from the center of the plasma to the chamber walls and from gas inlet to the nozzle exit assuming an axis-symmetric flow field.

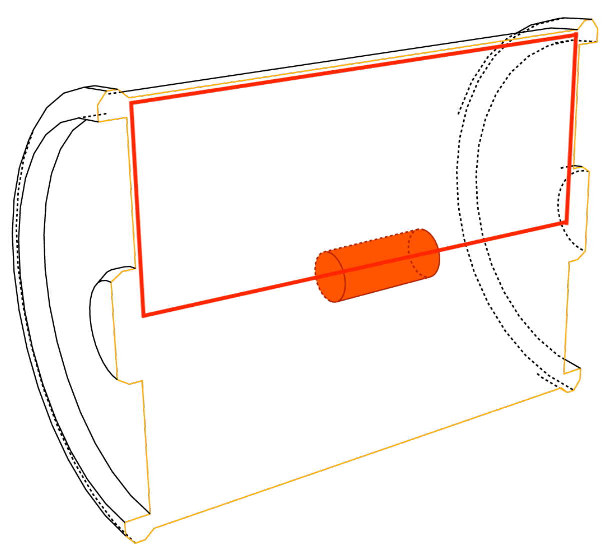

Figure 3.2: Highlighted Region of Interest for 2D Simulation

The temperature profile of the LSC can be solved by applying the conservation laws to the two-dimensional grid above.

Conservation of Mass

The conservation of mass for a two-dimensional system in cylindrical coordinates states:

$$\frac{\partial}{\partial t}(\rho) + \frac{\partial}{\partial z}(\rho u) + \frac{1}{r}\frac{\partial}{\partial r}(r\rho v) = 0, \tag{3.1}$$

where t is time, ρ is the gas density, u is the axial flow velocity, r is the radial position and v is the radial flow velocity.

However, this steady-state model makes use of the assumption that radial flow velocity is zero because it is almost negligible when compared to the axial flow velocity, so no radial flow or convection is permitted in the model. This allows the conservation of mass equation to be simplified to:

$$\rho u = \text{constant}. \tag{3.2}$$

Conservation of Momentum

With the assumption of a constant pressure flow field, the conservation of momentum equation becomes trivial to the system.

Conservation of Energy

The conservation of energy is the only equation from the conservation laws that requires a solution:

$$\frac{\partial}{\partial z}\left[k\frac{\partial T}{\partial z}\right] + \frac{1}{r}\frac{\partial}{\partial z}\left[rk\frac{\partial T}{\partial r}\right] - \rho u c_p \frac{\partial T}{\partial z} + \alpha I - \epsilon = 0, \tag{3.3}$$

where k is the thermal conductivity, c_p is the heat capacity, α is the absorption coefficient, I is the laser intensity and ϵ is the emission coefficient. k, c_p, α and ϵ are all a function of temperature, and their values are tabulated in the appendix section.

The conservation of energy equation is a balance between conductive, convective and radiative heat transfers inside the heating chamber that balances each other out for each element of the grid at steady state condition.

Boundary Conditions

The LSC model is bound on all four sides by different boundary conditions:

1. The upstream inlet boundary ($z = 0$) is a constant temperature boundary where $T = 300$ K. The hydrogen gas is assumed to enter the heating chamber at a uniform temperature of 300 K.

2. The downstream exit boundary ($z =$ heating chamber length) is assumed to have a negligible conductive heat transfer: $\frac{\partial T}{\partial z} = 0$.

3. The bottom boundary ($r = 0$) is a symmetric boundary condition: $\frac{\partial T}{\partial r} = 0$.

4. The top boundary ($r =$ chamber radius) is assumed to be far away enough from the heated center that it will not affect the system and vice versa, thus it will be assumed to be constant at 300 K ($T = 300$ K).

3.3.3 Beam Profile

The input laser is modelled as a convergent beam with a linearly increasing intensity along the radial axis. The beam is modelled with a variable focus and focus point to allow testing with various beam geometries. Once past the focus, the beam starts to diverge again until it reaches the chamber wall where it will propagate parallel to the walls as it makes the modelling easier.

In order to account for the attenuation of the laser beam as it travels through the hydrogen gas, the Beer-Lambert law is applied to the intensity of the laser as it moves along the axial direction:

$$\frac{dI}{dz} = -kI. \tag{3.4}$$

Ray tracing was not implemented into the beam geometry. Every update of the laser intensity is done by averaging out the intensity over the same linear distribution described above, which could cause the temperature profile to be overstated because the core area would absorb more. Nevertheless, this assumption allows for a less expensive implementation of the simulation while still providing an accurate picture of the heating chamber.

3.3.4 Solution

Assumptions

The key assumptions made that allowed this simulation to be possible were:

- Constant uniform pressure of 1 atm across the entire heating chamber.
- Negligible radial velocity and convective heat transfer in comparison to its axial counterpart.
- Radiation absorption between gases accounted for by conductive heat transfer coefficient.
- 1.06 μm laser radiation.
- Steady-state system.
- Axis-symmetric.

Solution Method

The temperature profile is solved by discretizing the region of interest and coupling the beam geometry to the conservation of energy equation, which creates a system of equations that can be solved by inverting the matrix.

However, due to the presence of nonlinear terms within the system as a result of radiation, the system must be solved through an iterative method and be allowed to converge to a solution. The temperature was solved through a successive overrelaxation (SOR) method where $w = 1.1$ was used as the relaxation parameter. The method is quite computationally expensive, especially for large grids on the order of 100 by 100, but provides good results (Figure 3.3) that can be well matched to existing theories on LSC waves.

It is important to note that a solution was obtained based on an initial temperature profile guess that was inputted into the SOR. While variances in the initial guess holds no impact on the final solved temperature, the initial guess must be greater than a threshold temperature of around 9000 K, under which the the model would be unable to absorb any of the incoming radiation and thus produce incorrect results.

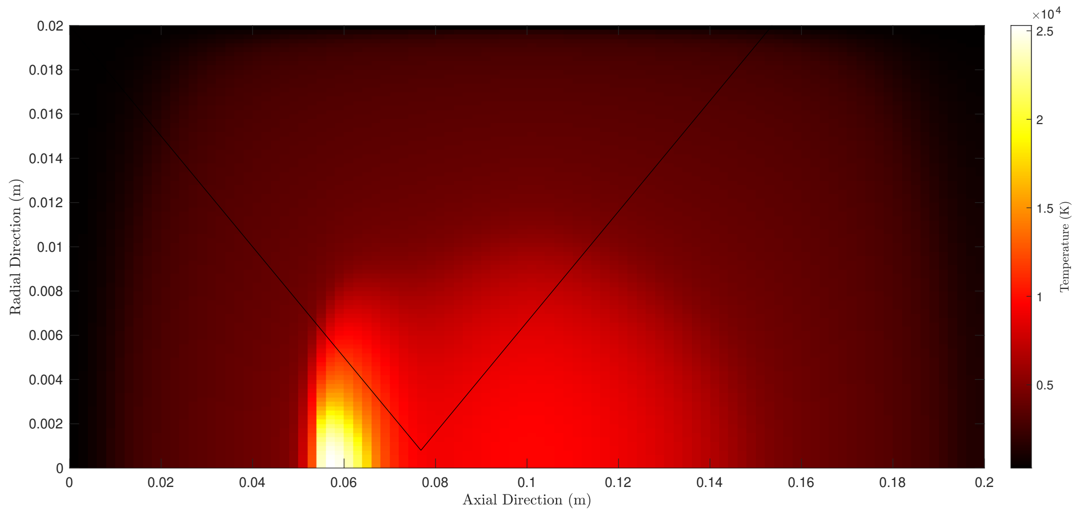

Figure 3.3: 100 kW Power Sustained Plasma with f/2 Focus (100 $\times$ 100 grid)

In Figure 3.3, the black line delimits the converging-diverging laser, and the three important plasma regions are very apparent. At the front of the plasma, there is a sharp rise in temperature that is characteristic of the pre-heating region where incoming cool hydrogen gas is rapidly heated by the plasma and becomes visible to 1 μm laser radiation. Following the pre-heating region is the absorption region where the hydrogen gas temperature is at its highest. This region absorbs the majority of incoming laser radiation, but also emits much of it to its surrounding. It is located in front of the focus rather than at the focus because the plasma will travel forward to stabilize at maintenance threshold laser intensity rather than at the maximum intensity possible. Finally, the hot plasma cools as the laser is not longer strong enough to maintain it, leaving a trail of hot hydrogen gas in the back. Expanding this hot gas before it cools through a large area ratio converging-diverging nozzle would enable higher exhaust velocities than those available on traditional chemical rockets, and thus by extension higher ΔV.

A smaller region of interest was selected for the analysis in order to focus on studying the interaction between the plasma and laser radiation rather than the inside of the heating chamber as a whole, which will be covered in greater detail in the following chapter. As alluded to in previous sections, cold hydrogen (below ionization temperature), is nearly invisible to radiation on a continuous wavelength basis and thus, a full scale heating chamber model will hold little value in providing further insight into the temperature profile of the entire heating chamber. For instance, Figure 3.3 was conducted on a 0.2 m by 0.02 m region, and the temperature in the surrounding decreases very quickly to around 500 K, where laser radiation cannot affect the gas anymore and would be pointless to model in a radiation dominated system.

3.3.5 Laser Power Input

The two-dimensional LSC model can provide insight into the effects of increasing laser power coupled to the heating chamber. Under similar operating conditions, an increase in power by an order of magnitude from 100 kW (Figure 3.4) to 1 MW (Figure 3.5) can result in significant increase in gas temperature. Furthermore, this increase also affects the shape and position of the plasma. Due to the increased intensity of the laser, the plasma propagates further forward to stabilize further forward at a the maintenance intensity and also becomes larger.

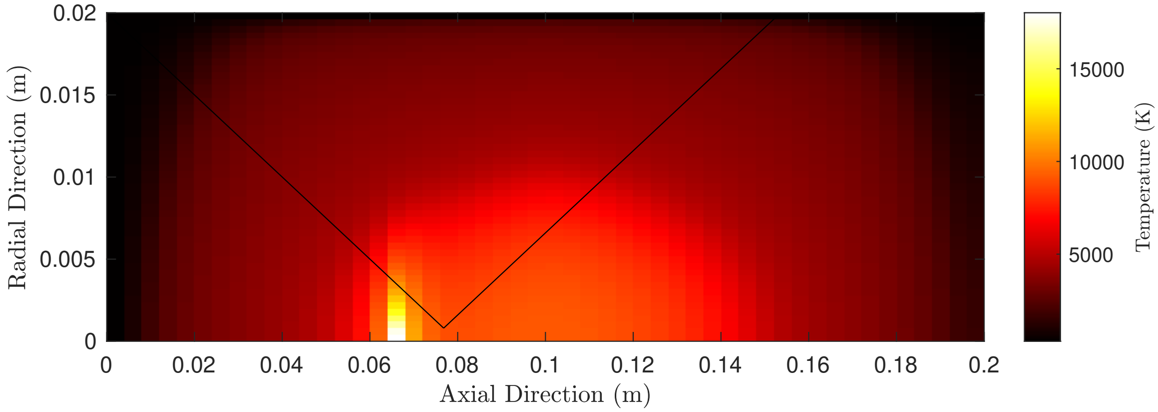

Figure 3.4: 100 kW laser input plasma (50 × 50 grid)

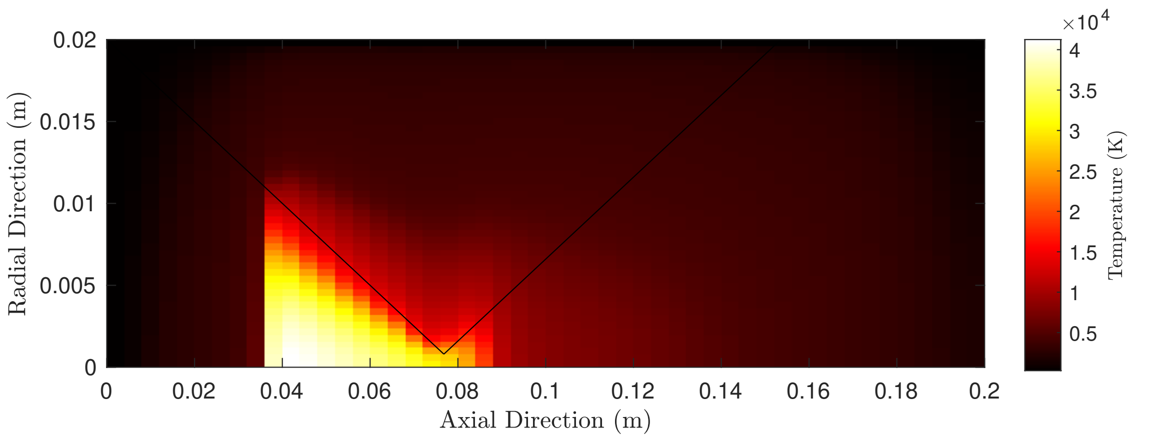

Figure 3.5: 1 MW laser input plasma

Chapter 4

Radiation Considerations

A potential weakness of laser thermal propulsion that has not been particularly addressed in its modelling and simulation is the shielding of the hardware on board from isotropic radiation emitted from high temperature gas in the middle. High temperature gas emits significantly to its surrounding (Figure 4.1) and, if not properly attenuated, can cause damage to peripheral components such as the chamber walls or other critical hardware.

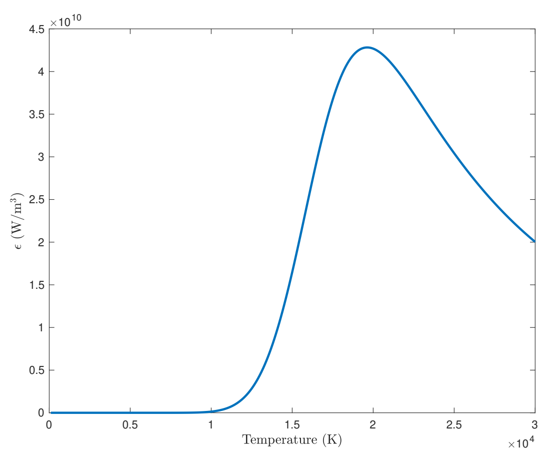

Figure 4.1: Hydrogen Volumetric Emissive Power

4.1 Solution Attempts

Solutions to this problem have been investigated numerically by Jeng [17] and experimentally by Shoji and Larson [19]. Jeng concluded that through a forced convective flow, the absorption of plasma can be improved to 100% and its emission loss down to 35%. Shoji and Larson build on top of that and suggests shielding in the form of carbon seeding of the working fluid to allow for radiation attenuation, which have shown to reduce radiation to the chamber walls down to 5%. In light of their experiments, this study has opted to implement a Monte Carlo simulation with participating media [20], [21] to investigate the impact of seeding not only on the chamber walls, but also on the surrounding gas.

4.1.1 Monte Carlo Simulations

Monte Carlo simulations use a random number approach to emulate particle transport. In the case of this investigation, it will be applied to track energetic radiation bundles as they travel through the working fluid from one surface to another. The position and direction of emission are all governed through random number relations that factor into account the properties of the surface and participating media.

4.2 Results

4.2.1 Assumptions

Monte Carlo simulations are expensive by nature. Thus simplifications were brought to the system for better computational time:

- Axis-symmetric and front/back symmetry of cylindrical heating chamber (region of interest highlighted in Figure 4.2)

- Radiative heat transfer dominated inside and outside heating chamber (The chamber walls are assumed to radiate on both sides – inwards towards the working fluid and outwards towards vacuum)

- Plasma assumed cylindrical, isothermal and black at 15000 K (0.01 m in radius and 0.1 m in length). It is opaque enough to be modelled as a surface emitter and not a volume emitter.

- Non-scattering gray participating media (constant κ or absorption coefficient)

- Chamber walls are black and not isothermal. They will be discretized into 0.05 m sections.

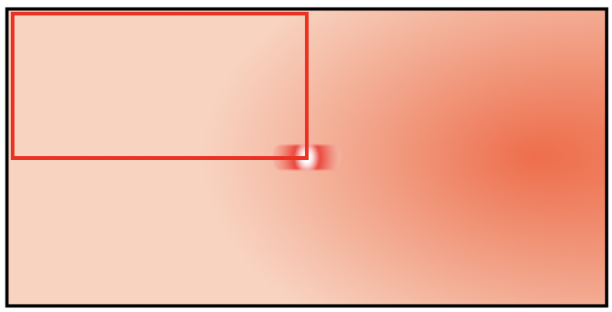

Figure 4.2: Region of Interest for Monte Carlo Simulation

This set of assumptions provides boundaries for the simulation as described by Figure 4.3. Both black surfaces (plasma and chamber walls) will absorb all bundles and also emit bundles of their own. The symmetric boundary is implemented into the simulation by modelling it as a perfectly specular reflective surface. The non-scattering gray gas is discretized into 0.05 m by 0.05 m regions and will reemit any energy bundles it absorbs to ensure conservation of energy is satisfied.

4.2.2 Wall and Gas Temperature Profile

A Monte Carlo simulation with 300,000 emitted bundles from the plasma and 30,000 emitted from each wall subsurface was executed with varying κ to compare the advantages of seeding the working fluid. A low absorption coefficent ($\kappa = 10$ m^{-1}) Monte Carlo simulation

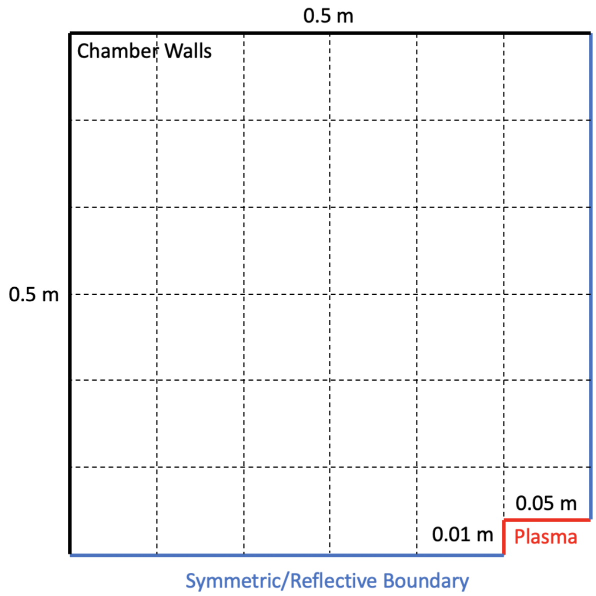

Figure 4.3: Monte Carlo Simulation Boundaries

to represent unseeded gas resulted in chamber wall temperatures between 5000 – 7000 K (Figure 4.4a), a temperature range where almost no material can maintain its shape. On the other hand, increasing the value of the absorption coefficient to 200 m^{-1} brought the wall temperature down to more reasonable levels between 200 – 1000 K (Figure 4.4b). The increase in absorption coefficient has a lesser impact on the temperature distribution of the participating media itself. In Figure 4.5, the two runs' maximum temperature barely differ, but the high temperature gas appears to be much more localized to the center, which would be very advantageous in shielding the wall from radiation damage.

The Monte Carlo simulation provides insight into the advantages of seeding the working fluid, which can be extremely beneficial in helping contain high radiation intensities emanating from the center of the heating chamber. The results shown in Figure 4.4 provides confidence from a design standpoint in containing the radiation loss towards the walls. Coupled with regenerative cooling, seeding the working fluid could act as a shield for the chamber walls and enhance efficiency by recovering lost enthalpy back into the working fluid for expansion.

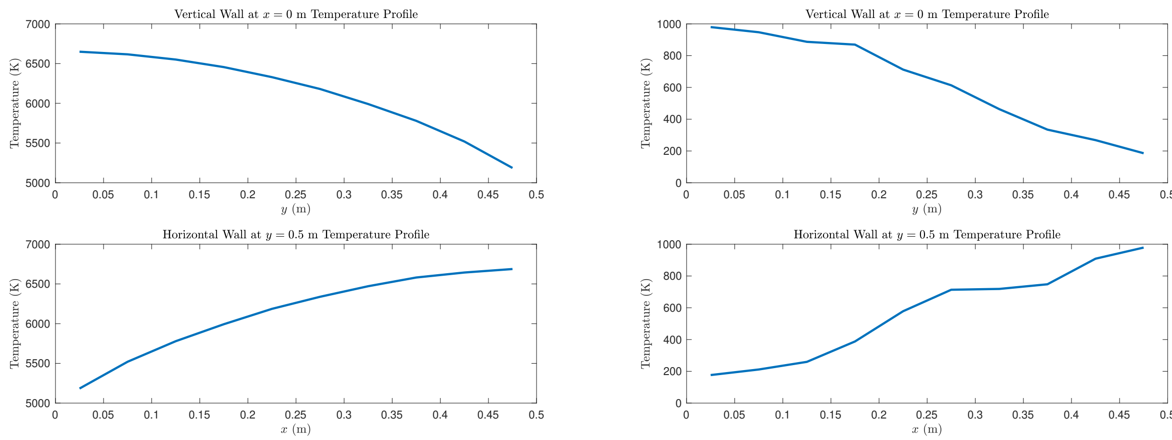

(a) $\kappa = 10$ m^{-1}

(b) $\kappa = 200$ m^{-1}

Figure 4.4: Chamber Wall Temperatures for Varying κ Values

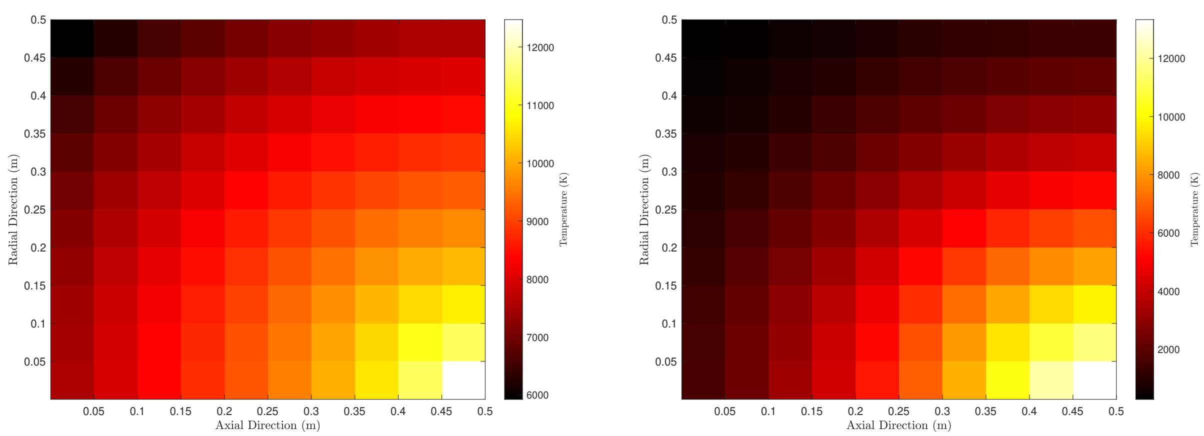

(a) $\kappa = 10$ m^{-1}

(b) $\kappa = 200$ m^{-1}

Figure 4.5: Participating Media Temperature Profile for Varying κ Values

4.3 Statistical Analysis

Despite the promising results, a stark difference can be observed between the variance of both test cases in Table 4.1, which can be explained by the lack of consideration for other forms in heat transfer in this model. As the wall temperature decreases to between 200 – 1000 K, black surface radiation can no longer properly capture the heat transfer mechanisms at the chamber wall boundaries because conductive and convective heat transfer both become relevant as well.

κ (m^{-1})	σ_{wall}	σ_{wall}
10	0.5902	0.9857
200	78.83	9.72

Table 4.1: Monte Carlo Variance

Chapter 5

Conclusion

In this thesis, the thrust and specific impulse considerations and heating chamber simulation of laser thermal propulsion were brought up-to-date for 1-μm fiber optic lasers from prior work conducted in the 1970s and 1980s. In light of this potentially disruptive technology for deep space propulsion applications, it was demonstrated that laser thermal propulsion could be a strong contender for near term applications of an eventual 10 m diameter laser array given that several of the issues alluded to within this thesis be addressed.

Simulations of the heating chamber were conducted from two different approaches in order to demonstrate the ability of laser thermal propulsion to capture incident radiation and to convert it into thrust. The fluid simulation demonstrated the possibility of achieving temperatures on the order of 10,000 K by coupling the laser to a working fluid, that would ideally be hydrogen. Furthermore, a Monte Carlo approach was taken to compute the temperature profile of the heating chamber walls and the participating gas, and addressed the concern of radiation damage to peripheral components of the rocket through seeding.

The numerical analysis show promising results in generating an I_{sp} on the order of 1000 s for laser thermal propulsion.

5.1 Future Work

To raise the technological readiness level of laser thermal propulsion going forward, further work must be done in refining the developed models. Stability and convergence studies should be conducted on the fluid simulation, and improvements should be brought to the Monte Carlo simulation such as the inclusion of other heat transfer mechanisms (regenerative cooling) and addition of spectral bands to the emitted bundles to account for true properties of the materials. If possible numerical results should be validated against experimental setups as well. Eventually, the Monte Carlo simulation should be coupled to the fluid simulation in order to reconcile both models to develop a more accurate picture of the temperature profile inside the heating chamber.

Bibliography

[1] P. Lubin, "A roadmap to interstellar flight," *Journal of the British Interplanetary Society*, vol. 69, pp. 40–72, 2016.

[2] J. Brophy, J. Polk, L. Alkalai, B. Nesmith, J. Grandidier, and P. Lubin, "A breakthrough propulsion architecture for interstellar precursor missions: Phase i final report," NASA, Tech. Rep., 2018.

[3] J. T. Kare, "Pulsed laser thermal propulsion for interstellar precursor missions," in *AIP Conference Proceedings*, AIP, vol. 504, 2000, pp. 1278–1284.

[4] H. Krier and R. Glumb, "Concepts and status of laser-supported rocket propulsion," *Journal of Spacecraft and Rockets*, vol. 21, no. 1, pp. 70–79, 1984.

[5] R. Conrad, C. Pyles, E. Roy, and D. Mangum, "Laser-supported combustion wave ignition in hydrogen.," Army Missile Command Redstone Arsenal AL Directed Energy Directorate, Tech. Rep., 1979.

[6] R. Welle, D. Keefer, and C. Peters, "Laser-sustained plasmas in forced argon convective flow. i-experimental studies," *AIAA Journal*, vol. 25, no. 8, pp. 1093–1099, 1987.

[7] J. R. Cook, "Laser propulsion—is it another myth or a real potential?" In *AIP conference proceedings*, AIP, vol. 997, 2008, pp. 109–118.

[8] P. E. Nebolsine and A. N. Pirri, "Laser propulsion: The early years," in *AIP Conference Proceedings*, AIP, vol. 664, 2003, pp. 11–21.

[9] J. Jackson and P. Nielsen, "Role of radiative transport in the propagation of laser supported combustion waves," *AIAA Journal*, vol. 12, no. 11, pp. 1498–1501, 1974.

[10] J. Mallinckrodt, "F does not equal d (mv)/dt," *The Physics Teacher*, vol. 48, no. 6, pp. 360–360, 2010.

[11] T. Benson, *Ideal rocket equation*, [Online; accessed 01-July-2019], 2014. [Online]. Available: `https://www.grc.nasa.gov/WWW/K-12/rocket/rktpow.html`.

[12] *Mission analysis for electric propulsion*, 2015.

[13] N. Kemp, R. Root, P. Wu, G. Caledonia, and A. Pirri, "Laser-heated rocket studies," Physical Sciences Inc Andover, MA, Tech. Rep., 1976.

[14] L. J. Radziemski and D. A. Cremers, *Laser-induced plasmas and applications*. Marcel Dekker Inc., 1989.

[15] N. H. Kemp and R. G. Root, "Analytical study of laser-supported combustion waves in hydrogen," *Journal of Energy*, vol. 3, no. 1, pp. 40–49, 1979.

[16] D. Keefer, C. Peters, and H. Crowder, "A re-examination of the laser-supported combustion wave," *AIAA Journal*, vol. 23, no. 8, pp. 1208–1212, 1985.

[17] S.-M. Jeng, D. R. Keefer, R. Welle, and C. E. Peters, "Laser-sustained plasmas in forced convective argon flow. ii-comparison of numerical model with experiment," *AIAA Journal*, vol. 25, no. 9, pp. 1224–1230, 1987.

[18] R. GLUMB and H. KRIER, "Two-dimensional model of laser-sustained plasmas in axisymmetric flowfields," *AIAA journal*, vol. 24, no. 8, pp. 1331–1336, 1986.

[19] J. Shoji and V. Larson, "Performance and heat transfer characteristics of the laser-heated rocket-a future space transportation system," in *12th International Electric Propulsion Conference*, 1976, p. 1044.

[20] J. R. Howell, "The monte carlo method in radiative heat transfer," *Journal of Heat Transfer*, vol. 120, no. 3, pp. 547–560, 1998.

[21] J. R. Howell, M. P. Menguc, and R. Siegel, *Thermal radiation heat transfer*. CRC press, 2015.

[22] R. Patch, "Thermodynamic properties and theoretical rocket performance of hydrogen to 100,000 k and 1.01325 x 10 to the 8th power n/sq m," NASA, Tech. Rep., 1971.

[23] N. T. Grier, "Calculation of transport properties of ionizing atomic hydrogen," NASA, Tech. Rep., 1966.

[24] ——, "Calculation of transport properties and heat transfer parameters of dissociating hydrogen," NASA, Tech. Rep., 1962.

[25] Y. B. Zel'Dovich and Y. P. Raizer, *Physics of shock waves and high-temperature hydrodynamic phenomena*. Courier Corporation, 2012.

[26] L. D. Landau and E. M. Lifshitz, "The classical theory of fields," 1962.

Appendix A

Property Fits and Calculations

This appendix documents the methods used to obtain specific heat, absorption length, thermal conductivity and radiation loss of hydrogen at different temperatures. In order to properly account for the dissociation and ionization effects of hydrogen, a switch was incorporated into the model [15]:

$$T^* = 2000\ \log_{10}(P\ (\text{in atm})) + 7000, \tag{A.1}$$

where if $T \geq T^*$, then it is assumed all hydrogen has fully dissociated. On the other hand, if $T < T^*$, then it is assumed no ionization effects take place.

A.1 Dissociation vs. Ionization

The ionization and dissociation ratios are calculated in different ways depending on the temperature based on Kemp's study [13].

$$\theta_{\mathrm{I}} = 158000\ \mathrm{K} \tag{A.2}$$

$$\theta_{\mathrm{r}} = 87.62\ \mathrm{K} \tag{A.3}$$

$$\theta_{\mathrm{v}} = 5983\ \mathrm{K} \tag{A.4}$$

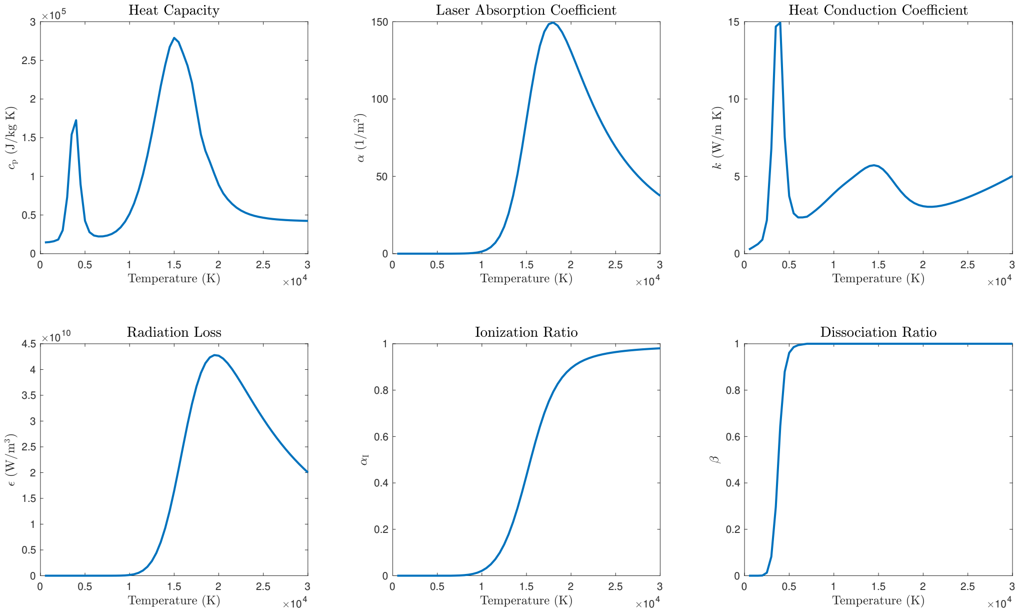

Figure A.1: Variation of properties over temperature

$$\theta_{\mathrm{D}} = 52000 \text{ K} \tag{A.5}$$

$$S_1 = \sum_{n=1}^{17} n^2 \exp\left(\frac{\theta_{\mathrm{I}}}{Tn^2}\right) \tag{A.6}$$

For $T \geq T^*$:

$$\beta = 1 \tag{A.7}$$

$$f_I = \left(\frac{2\pi m_{\mathrm{E}} k}{{h_{\mathrm{P}}}^2}\right)^{3/2} \frac{kT^{5/2}}{S_1} \tag{A.8}$$

$$\alpha = \left(1 + \frac{P \text{ (in Pa)}}{f_{\mathrm{I}}}\right)^{-1/2} \tag{A.9}$$

For $T < T^*$:

$$\alpha = 0 \tag{A.10}$$

$$f_D = \left(\frac{\pi m_{\mathrm{A}} k}{{h_{\mathrm{P}}}^2}\right)^{3/2} 2k\theta_{\mathrm{r}} T^{3/2} (1 - \exp(-\theta_{\mathrm{v}}/T)) \exp(-\theta_{\mathrm{D}}/T) \tag{A.11}$$

$$\beta = \left(1 + \frac{P \text{ (in Pa)}}{f_{\mathrm{D}}}\right)^{-1/2} \tag{A.12}$$

where α is the ionization ratio, β is the dissociation ratio, θs are state temperatures of hydrogen, f_I and f_D are function definitions. m_E is the electron mass and m_A is the hydrogen atom mass:

$$m_\mathrm{E} = 9.109 * 10^{-31} \text{ kg} \tag{A.13a}$$

$$m_\mathrm{A} = 1.673 * 10^{-27} \text{ kg} \tag{A.13b}$$

k is the Boltzmann constant and h_P is the Planck constant:

$$k = 1.38064852 * 10^{-23} \ \frac{\mathrm{J}}{\mathrm{K}} \tag{A.14a}$$

$$h_\mathrm{P} = 6.62607015 * 10^{-34} \ \mathrm{J} * \mathrm{s} \tag{A.14b}$$

A.2 Specific Heat

The specific heat of the system is obtained by taking the cubic spline of Patch's tables on thermodynamic properties for 1 atm [22].

A.3 Thermal Conductivity

The thermal conductivity is interpolated using a cubic spline from Grier's tables. For $T \geq T^*$, Grier's tables on ionizing hydrogen [23] is interpolated, and for $T < T^*$, Grier's tables on dissociating hydrogen [24] is used instead.

A.4 Absorption Length

Absorption length (in m^{-1}) is modeled based on the following equations [13]:

$$k_\mathrm{LEI} = 8.7 \times 10^8 \ \alpha^2 \ \beta^2 \ \frac{\rho_0^2}{\sqrt{T}} \ (\exp{(13570/T)} - 1) \tag{A.15a}$$

$$Q_{\mathrm{EN}} = \frac{2.96 \times 10^{-45} T}{1 - \exp \frac{-h_{\mathrm{P}}\ c}{\lambda\ k\ T}}\ (\frac{\theta_{\mathrm{I}}\ k\ \lambda}{h_{\mathrm{P}}\ T\ c})^2\ \sqrt{\theta_{\mathrm{I}}/T} \tag{A.15b}$$

$$k_{\mathrm{LEN}} = 4\ Q_{\mathrm{EN}}\ \alpha\ (1-\alpha)\ \rho_0\ \sqrt{T}\ (1 - \exp(\frac{-h_{\mathrm{P}}\ c}{\lambda\ k\ T}))/10^{-4} \tag{A.15c}$$

$$k_{\mathrm{L}} = k_{\mathrm{LEI}} + k_{\mathrm{LEN}} \tag{A.15d}$$

where c is the speed of light, Q_{EN} is the absorption cross-section, k_{LEI} is the absorption coefficient for electron-ion absorption and k_{LEN} is the absorption length for electron-neutral absorption. k_{L} is the total absorption coefficient.

A.5 Radiation Loss

The radiation loss model is derived based on Zel'Dovich and Raizer's treatment of gas absorption and emission at high temperature [25].

Consideration for emission will only be given to bound-free and free-free electron transitions because contributions from line emissions are minimal and neglecting them will not affect results.

A.5.1 Bremsstrahlung

The energy emitted by electrons with velocities between v' and $v'+dv'$ and frequency between ν and $\nu + d\nu$ per unit time and per unit volume is:

$$N_+\ N_e\ f(v')\ dv'\ v'\ dq_\nu(v'), \tag{A.16}$$

where N_+ is the positive ion number denisty, N_e is the electron number density, $f(v')$ is the Maxwell velocity distribution:

$$f(v') = 4\pi \left(\frac{m}{2\pi kT}\right)^{3/2} v'^2 exp\left(\frac{-mv'^2}{2kT}\right), \tag{A.17}$$

where m is the electron mass, and $dq_\nu(v')$ is the effective radiation term derived by Landau and Lifshitz [26] and is described by:

$$dq_\nu(v') = \frac{32\pi^2 Z^2 e^6}{3\sqrt{3} m^2 c^3 v'^2} d\nu, \tag{A.18}$$

where Z is the atomic number, e is the electron charge and c is the speed of light.

Integrating from the minimum velocity without being absorbed ($\frac{1}{2} m v_{\rm min}^2 = h_{\rm P}\nu \Rightarrow v_{\rm min} = \sqrt{\frac{2h_{\rm P}\nu}{m}}$) to ∞ gives the energy emission for a wavelength interval per unit time and per unit volume:

$$\epsilon_\nu d\nu = \frac{32\pi}{3}\left(\frac{2\pi}{3mkT}\right)^{1/2} \frac{Z^2 e^6}{mc^3} N_+ N_e e^{-\frac{h\nu}{kT}} d\nu \tag{A.19}$$

Then, integrating wavelengths from 0 to ∞ for the total contribution from free-free transitions:

$$\epsilon_{\rm FF} = \frac{32\pi}{3}\left(\frac{2\pi kT}{3m}\right)^{1/2} \frac{Z^2 e^6}{mc^3 h} N_+ N_e. \tag{A.20}$$

A.5.2 Photoelectric Effect

The radiative capture of electrons with velocities between v and $v + dv$ into the nth ionic level per unit volume per unit time is:

$$N_+ \; N_e \; f(v) \; dv \; v \; \sigma_{cn}, \tag{A.21}$$

where $\sigma_{\rm cn}$ is the cross-section into level n for a free electron:

$$\sigma_{\rm cn} = \frac{128\pi^4}{3\sqrt{3}} \frac{Z^4 e^{10}}{mc^3 h^4 v^4 \nu} \frac{1}{n^3}. \tag{A.22}$$

The energy emitted by electrons with velocities between v and $v + dv$ into the nth ionic level per unit volume per unit time is:

$$N_+ \; N_e \; f(v) \; dv \; v \; \sigma_{cn} \; \left(\frac{mv^2}{2} - E_n\right), \tag{A.23}$$

where E_n is the energy level the electron was captured into described by:

$$E_n = -hcR_\infty \frac{Z^2}{n^2} = -\frac{13.6Z^2}{n^2}. \tag{A.24}$$

Taking advantage of the relation to simplify:

$$h\nu = E - E_n = \frac{mv^2}{2} - E_n, \tag{A.25}$$

and integrating over all velocities:

$$\epsilon_n = N_+ \; N_e \; 4\pi \left(\frac{m}{2\pi kT}\right)^{3/2} \frac{128\pi^4}{3\sqrt{3}} \frac{Z^4 e^{10}}{mc^3h^3} \frac{1}{n^3} \frac{kT}{m}. \tag{A.26}$$

Finally, summing over all energy levels gives the contribution to emission from bound-free transitions:

$$\epsilon_{BF} = 1.2021 N_+ \; N_e \; \frac{256\pi^4}{3\sqrt{6}} \left(\frac{1}{\pi mkT}\right)^{1/2} \frac{Z^4 e^{10}}{c^3h^3} \tag{A.27}$$

A.5.3 Total Emissive Power

The total emissive power (in $\frac{\mathrm{W}}{\mathrm{m}^3}$) is obtained by summing both contributions from bound-free (Eqn. A.27) and free-free (Eqn. A.20) transitions:

$$\epsilon = N_+ N_e \left(\frac{32\pi}{3} \left(\frac{2\pi kT}{3m}\right)^{1/2} \frac{Z^2 e^6}{mc^3 h} + 1.2021 \, \frac{256\pi^4}{3\sqrt{6}} \left(\frac{1}{\pi mkT}\right)^{1/2} \frac{Z^4 e^{10}}{c^3h^3} \right) \tag{A.28}$$

N_+ and N_e are assumed to be equal and can be obtained by solving the Saha equation:

$$\frac{N_+ \; N_e}{N} = 2 \left(\frac{2\pi mkT}{h^2}\right)^{3/2} \frac{u_+}{u} \exp\left(-I/kT\right) \tag{A.29}$$